Design, Isolation, and Spectroscopic Analysis of a Tetravalent Terbium Complex

Natalie T. Rice,[†] Ivan A. Popov,[‡] Dominic R. Russo,[†] John Bacsa,[†] Enrique R. Batista,[‡] Ping Yang,[‡] Joshua Telser,[§] and Henry S. La Pierre[†,ϕ*]

[†] School of Chemistry and Biochemistry, Georgia Institute of Technology, Atlanta, Georgia 30332-0400, United States.

[‡] Theoretical Division, Los Alamos National Laboratory, Los Alamos, New Mexico 87545, United States.

[§] Department of Biological, Chemical and Physical Sciences, Roosevelt University, Chicago, Illinois 60605, United States.

[ϕ] Nuclear and Radiological Engineering and Medical Physics Program, School of Mechanical Engineering, Georgia Institute of Technology, Atlanta, Georgia 30332-0400, United States.

Supporting Information Placeholder

ABSTRACT: Synthetic strategies to yield molecular complexes of high-valent lanthanides, other than the ubiquitous Ce^{4+} ion, are exceptionally rare, and thorough, detailed characterization in these systems is limited by complex lifetime and reaction and isolation conditions. The synthesis of high-symmetry complexes in high purity with significant lifetimes in solution and solid-state are essential for determining the role of ligand-field splitting, multiconfigurational behavior, and covalency in governing the reactivity and physical properties of these potentially technologically transformative tetravalent ions. We report the synthesis and physical characterization of an S_4 symmetric, four-coordinate tetravalent terbium complex, [Tb(NP(1,2-bis-^{t}Bu-diamidoethane)(NEt_2))$_4$] (where Et is ethyl and *t*Bu is *tert*-butyl). The ligand field in this complex is weak and the metal-ligand bonds sufficiently covalent so that the tetravalent terbium ion is stable and accessible via a mild oxidant from the anionic, trivalent, terbium precursor, [(Et_2O)K][Tb(NP(1,2-bis-^{t}Bu-diamidoethane)(NEt_2))$_4$]. The significant stability of the tetravalent complex enables its thorough characterization. The step-wise development of the supporting ligand points to key ligand control elements for further extending the known tetravalent lanthanide ions in molecular complexes. Magnetic susceptibility, electron paramagnetic resonance (EPR) spectroscopy, X-ray absorption near-edge spectroscopy (XAS), and density functional theory studies indicate a $4f^7$ ground state for [Tb(NP(1,2-bis-^{t}Bu-diamidoethane)(NEt_2))$_4$] with considerable zero-field splitting: demonstrating that magnetic, tetravalent lanthanide ions engage in covalent metal-ligand bonds. This result has significant implications for the use of tetravalent lanthanide ions in magnetic applications since the observed zero-field splitting is intermediate between that observed for the trivalent lanthanides and for the transition metals. The similarity of the multiconfigurational behavior in the ground state of [Tb(NP(1,2-bis-^{t}Bu-diamidoethane)(NEt_2))$_4$] (measured by Tb L_3-edge XAS) to that observed in TbO_2 implicates ligand control of multiconfigurational behavior as a key component of the stability of the complex.

INTRODUCTION

In molecular complexes, the lanthanides are predominantly trivalent (Ln^{3+}). In fact, of the fifteen lanthanide ions, only cerium is known to have significant solution chemistry in its tetravalent oxidation state (Ce^{4+}).[1] While examples of low-valent lanthanide complexes have been reported,[2-6] high-valent ions in lanthanide chemistry remain a challenge.[7-11] The accessibility of high-valent lanthanide chemistry could transform two key industrial chemical processes: 1) the beneficiation and purification of lanthanide ores[12] and 2) the separation of the minor actinides from lanthanide fission products in spent nuclear fuel reprocessing.[13] As a result, efforts to extend the aqueous solution chemistry of tetravalent lanthanides to the next two most readily oxidized lanthanides, praseodymium and terbium (Pr^{4+}/Pr^{3+}= +3.2; Tb^{4+}/Tb^{3+}= +3.1 V vs. NHE),[14] have been pursued, but with little success beyond the *in situ* spectroscopic and potentiometric identification of redox processes.[15-17] From the most fundamental perspective, the isolation of a tetravalent terbium complex is important since it puts a new paramagnetic, isotropic ion on the periodic table and allows the crystal field effects in the tetravalent lanthanides to be benchmarked against the transition metals (Mn^{2+}) and trivalent lanthanides (Gd^{3+}).

In the absence of isolable molecular, tetravalent praseodymium or terbium complexes, cerium has been used as a surrogate to examine the ligand and solvent dependence of the Ln^{4+}/Ln^{3+} redox couple.[18-20] Depending on the ligand, supporting cation, and solvent, the redox potential can be shifted up to 4 V. Given the large change in ionic radii on oxidation from Ce^{3+} to Ce^{4+} (~ 0.14 Å),[21] the coordination sphere has also been demonstrated to have kinetic control of the redox process.[22] This ligand control has led to rapid growth of tetravalent cerium coordination chemistry.[23] The use of cerium as a surrogate is validated by the demonstration that tetravalent late-actinides, such as berkelium, can be preferentially stabilized using similar ligand design principles.[24, 25] These cerium coordination studies have also inspired the attempted oxidation of molecular terbium complexes in anaerobic and anhydrous conditions, but these efforts have failed in the isolation of a tetravalent terbium complex.[26-28] The limited data on the physical properties of tetravalent terbium are derived from studies on solid-state materials including doped-oxides (*e.g.* ThO_2:Tb^{4+}),[29, 30] bulk binary terbium oxides and fluorides (TbO_2 and TbF_4),[31, 32] and other extended solids.[33-37] Electron paramagnetic resonance (EPR) and X-ray absorption spectroscopy (XAS) studies of these solid-state terbium complexes and related tetravalent lanthanide and actinide complexes indicate that the increased covalent bonding present in

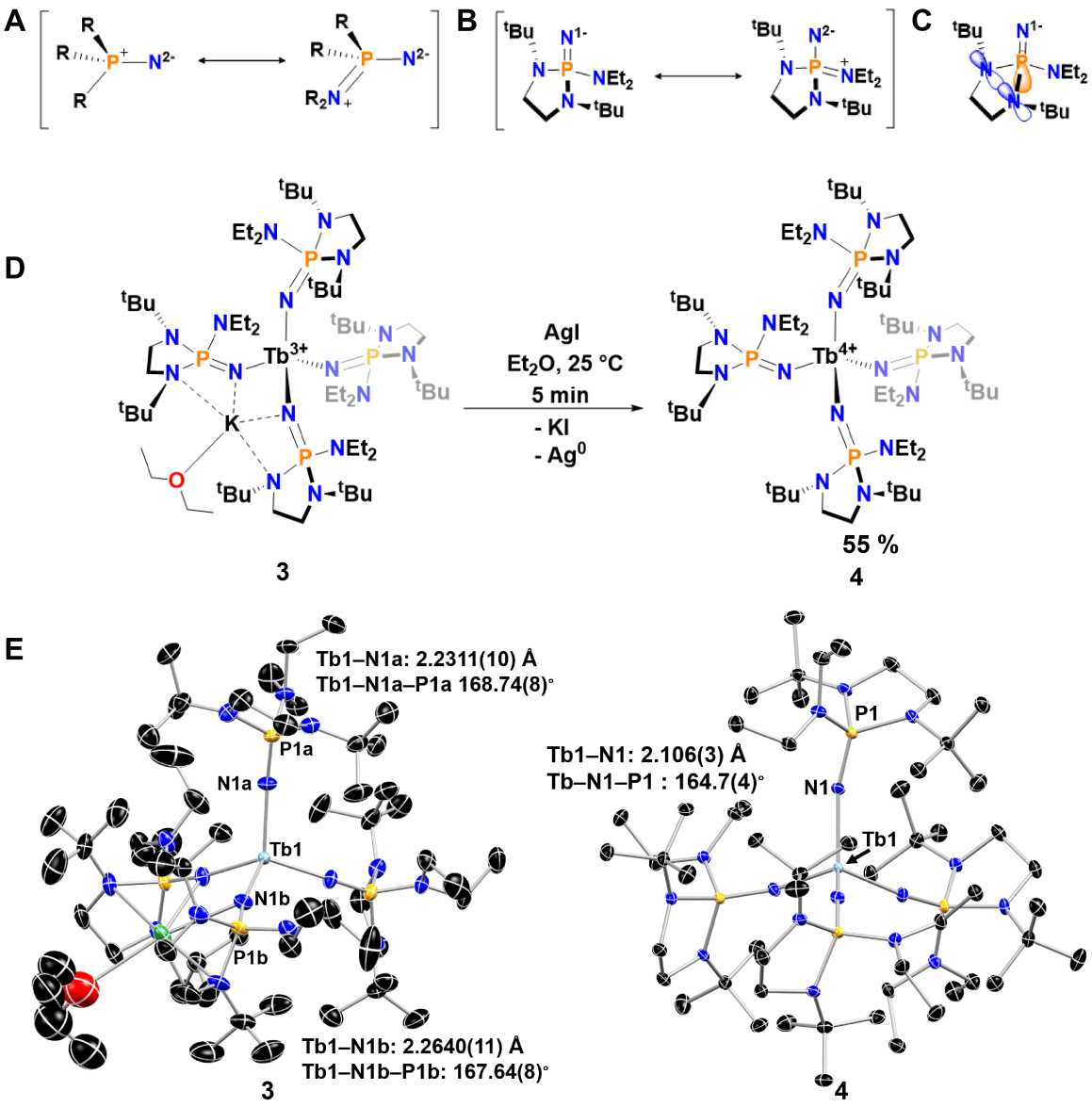

Figure 1. Synthesis and structure of terbium imidophosphorane complexes. (A) Resonance structures in *tris*(piperidinyl)imidophosphorane ligand. (B) Resonance structures in **2**. (C) Hyperconjugation in **2**. (D) Synthesis of **4** from **3**. (E) X-ray crystal structures of **3** and **4** with thermal ellipsoids at 50% probability. Black, blue, yellow, red, and aqua represent carbon, nitrogen, phosphorous, oxygen and terbium, respectively. Metrical data for Tb–N and P–N distances and Tb–N–P angles in each complex.

tetravalent *f*-block metal-ligand bonds can be employed to stabilize reactive tetravalent lanthanide ions.[29, 31, 36-39] Here, we report the synthesis and structural characterization of a molecular tetravalent terbium complex that is stable both in solution and the solid-state. Most importantly, the $4f^7$, $^8S_{7/2}$ ground state is validated and probed through EPR, Tb L_3-edge XAS, magnetic susceptibility, and density functional theory (DFT) studies.

RESULTS AND DISCUSSION

We recently reported the ability of the *tris*(piperidinyl)imidophosphorane, $[NP(pip)_3]^-$ (pip = piperidinyl), ligand to dramatically lower the redox potential for the $Ce^{3+/4+}$ couple by greater than 4 V to less than -2.64 V vs. Fc/Fc^+ (-2.99 V vs. Fc/Fc^+; DFT).[20] This control of the $Ce^{3+/4+}$ couple is driven by four key aspects of ligand design: 1) destabilization of the trivalent state through significant charge localization at the imide nitrogen atom due to the zwitterionic character of the ligand (Fig. 1A), 2) stabilization of the tetravalent product through significant covalent character in the metal-ligand bonds enabled by symmetry and energy allowed mixing, 3) minimization of complex structural reorganization during oxidation, and 4) increase of the thermodynamic driving force for oxidation via the release of a potassium ion from the secondary coordination sphere. Initially, the terbium analog of the trivalent cerium complex supported by $[NP(pip)_3]^-$ was prepared (reported in this work) to investigate its redox properties (SI). With the contraction of ionic radii across the lanthanide series (Ce^{3+}, 1.01 Å; Tb^{3+}, 0.92 Å),[21] the coordination geometry in $[(Et_2O)K][Tb(NP(pip)_3)_4]$, **1**, diverges from its previously reported cerium analog, $[(Et_2O)K][Ce(NP(pip)_3)_4]$, **1**–**Ce**.[20] The potassium ion hapticity is κ^3, supported by three ligands, in **1** as opposed to κ^2, supported by two ligands, in **1**–**Ce**. As a result, three of the

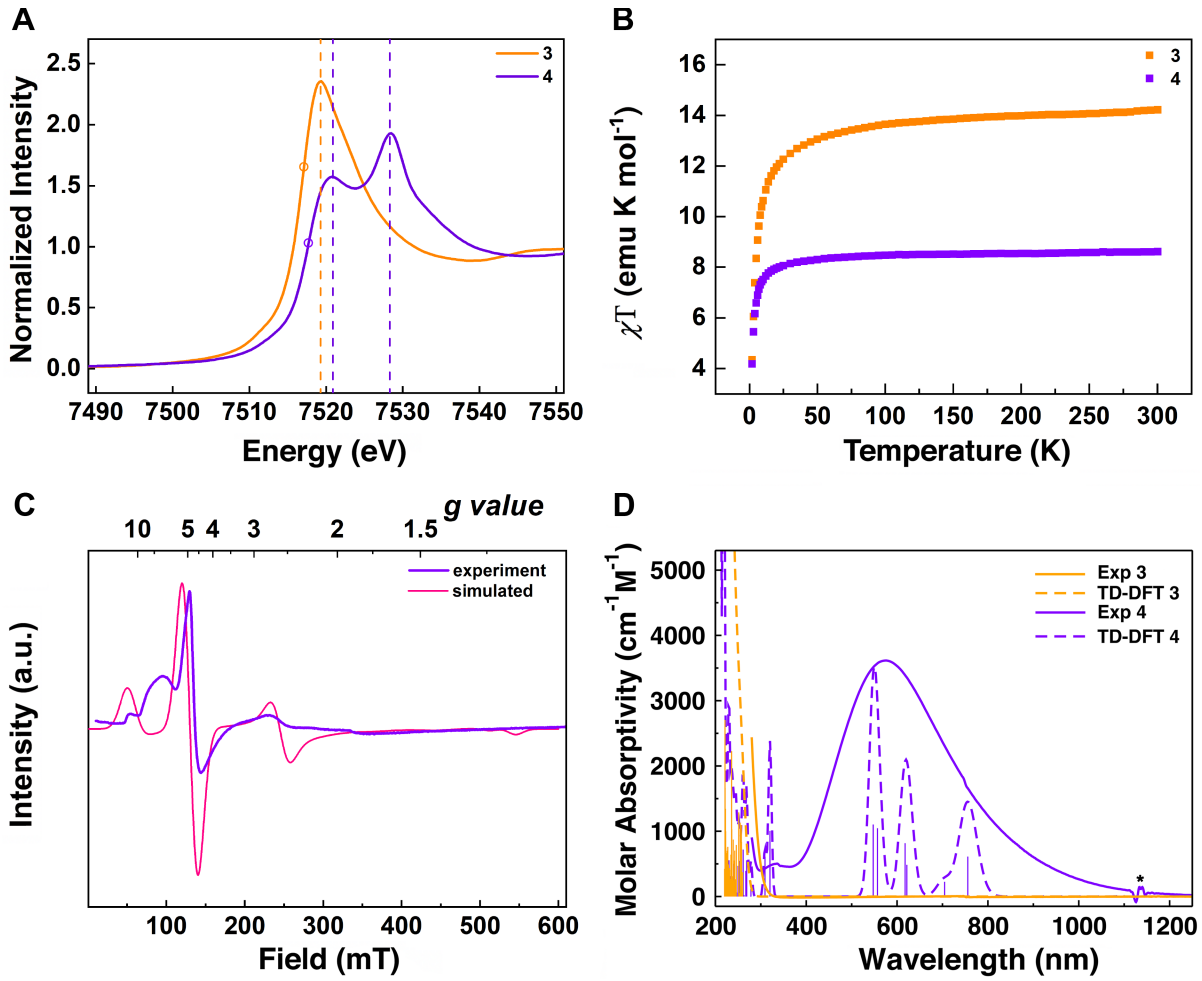

Figure 2. Spectroscopic and magnetic analysis of **3** and **4**. (A) Terbium L_3-edge X-ray absorption spectra of **3** and **4**. (B) Variable-temperature molar magnetic susceptibility times temperature ($\chi_M T$) for **3** and **4** collected under dc field (*H*) of 1 T. (C) X-band electron paramagnetic resonance spectrum of **4** in a toluene glass at 12 K. (D) Experimental UV/vis/NIR spectra of **3** and **4** in benzene (solid lines) and their computed TD-DFT spectra in the UV/vis region (dashed lines). Vertical bars depict theoretical oscillator strength of single-electron excitations.

imidophosphorane ligands are bent with Tb–N–P angles spanning the range 135.2(4) to 172.5(5)° (Fig. S23-24 and Table S6). This coordination geometry reduces electron donation to the metal and diminishes the destabilization of the *f*-orbitals in contrast to the κ^2-geometry observed in **1**–**Ce**. Additionally, this potassium coordination mode increases the amount structural rearrangement required to form a neutral tetravalent complex. In line with these structural observations (but not the redox chemistry of **1**–**Ce)**, no reactions are observed between **1** and mild oxidants such as AgI.

In light of the structural analysis of **1**, a new ligand architecture was developed to address the changes in coordination chemistry observed at trivalent terbium. A bulky, chelating diamide was incorporated into the imidophosphorane ligand (Fig. 1B and S1B). This change has two principal effects on the electronic structure of the imidophosphorane ligand. The chelating diamide enforces planarity at the chelating amide nitrogens and aligns their N lone pairs with the σ* orbital of the P–N_{imide} bond. This hyperconjugative interaction destabilizes the P–N_{imide} and makes the ligand more σ basic and is reflected in the increased in P–N_{imide} bond length of the potassium salt of the new ligand, K[NP(1,2-*bis*-^{t}Bu-diamidoethane)(NEt_2)], **2**, in comparison to that of the original ligand, K[NP(pip)$_3$] (Table S1 and Fig. S21-22). The chelating diamide sterically enforces the structural requirement for the zwitterionic resonance structure shown in Fig. 1B which increases the π basic character of the ligand. These electronic and steric modifications of the imidophosphorane ligand lead to significant changes in the coordination geometry of trivalent terbium. As seen in Fig. 1D, the potassium ion is bound κ^4 by two ligands in the tetrahomoleptic, trivalent, terbium complex [(Et_2O)K][Tb(NP(1,2-*bis*-^{t}Bu-diamidoethane)(NEt_2))$_4$], **3** (Fig. S25 and Tables S7-8). Additionally, since the potassium ion is bound by both an imide nitrogen and an amide nitrogen from each ligand, the Tb–N–P angle for the ligand binding the potassium ion is much more linear than in **1** at 167.64(8)°. This angle is comparable to that measured for the non-bridging ligand in **3** at 168.74(8)°. The Tb–N distances in **3** are also similar for the bridging and terminal imidophosphorane ligand (2.264(1) and 2.231(1) Å, respectively). These comparable geometries suggest that minimal complex reorganization is necessary upon oxidation.

Complex **3** oxidizes rapidly (< 10 min) with AgI in diethyl ether at room temperature to give a deep indigo solution, Ag^0, and a white precipitate. After filtration and crystallization from pentane at -35 °C, dark indigo crystals are isolated. Single-crystal X-ray diffraction studies of these crystals demonstrated the

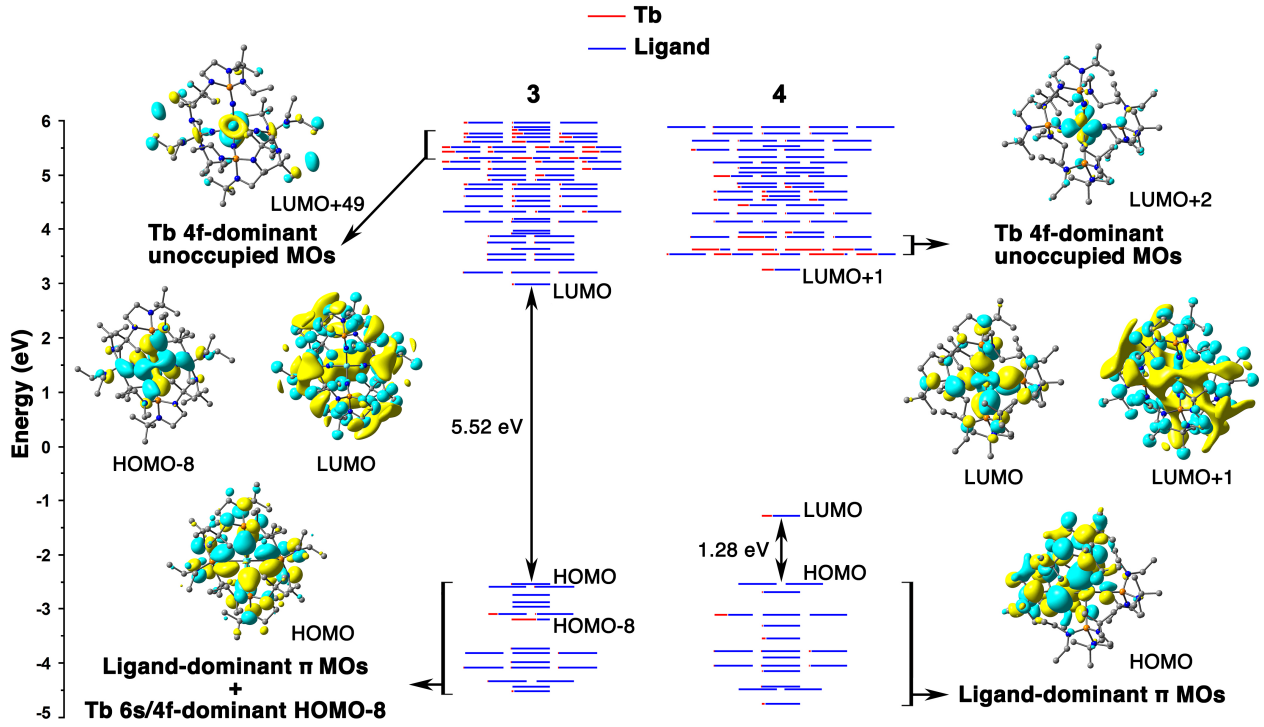

Figure 3. MO energy levels of **3** and **4**. Only β MOs are shown to explain the origin of the excitations in the low-energy region of **4**. HOMO level of **4** is shifted up by 2.37 eV to align with the HOMO of **3** for comparison. The red fraction of the MO lines represents the percentage of Tb AOs in the MOs, and the blue lines are the ligand fraction. Degeneracy of the MO energy levels is set to 0.05eV. Combined (α+β) MO diagrams are shown in Fig. S35

isolation of [Tb(NP(1,2-*bis*-^{t}Bu-diamidoethane)(NEt$_2$))$_4$], **4**, in 55% yield (Fig. 1D, Fig. S27, and Table S11-12). The Tb–N–P angle in **4** is 164.7(4)°, confirming that little rearrangement was necessary to accommodate the oxidation and concomitant contraction of the metal ionic radius. The Tb–N distance in **4** is 2.106(3) Å: a contraction of 0.164 Å and 0.133 Å for the terminal and bridging ligands in **3**, respectively. This contraction is consistent with a change in the ionic radius from Tb^{3+} to Tb^{4+} (Tb^{3+}, 0.92 Å; Tb^{4+}, 0.76 Å) and is strong crystallographic evidence that the observed oxidation is metal-centered. It should also be noted that the P–N_{imide} bond in **4** is slightly longer than the comparable bonds in **3** (1.555(3) Å compared to 1.528(1) and 1.532(1) Å in **3** or 1.526(7) (avg.) Å in **2**). This elongation could reflect increased electron donation to the metal in the oxidized complex.

The significant stability of these complexes facilitates the direct spectroscopic confirmation of the oxidation of trivalent terbium to tetravalent terbium in **4** via terbium L_3-edge XAS studies at 10 K. Figure 2A shows the background subtracted and normalized spectra of **3** and **4**. The spectrum of **3** (orange) contains a large edge feature at 7519.3 eV (inflection point, 7517.1 eV) superimposed on a step-like absorption threshold, typical of an L_3-edge spectrum of a trivalent lanthanide.[5] The spectrum of **4** (indigo) exhibits a double-peak structure characteristic of L_3-edge spectra obtained from other formally Ln^{4+} complexes.[31, 36-38, 40] The inflection point is shifted to higher energy by 0.8 eV and the two peak maxima are also shifted to higher energy (7520.9 and 7528.3 eV, 7.4 eV splitting) demonstrating increased effective nuclear charge at the absorbing atom. This double peak structure has been attributed to transitions from $4f^n5d^0L$ and $4f^{n+1}5d^0\underline{L}$ ground states to $4f^n5d^1L$ and $4f^{n+1}5d^1\underline{L}$ final states (where $\underline{L}$ represents a ligand hole).[20, 31, 38, 40] The fit of the spectrum, with Voigt functions and a step-like function (Fig. S45 and Table S17), was used to estimate the relative amount of $4f^{n+1}5d^0\underline{L}$ character in the ground state via a weighted ratio of area under the two peaks giving a value of 0.39(4), similar to that observed for TbO_2, 0.42(3).[31] The spectral features of **4** in comparison with **3** and other Ln^{4+} complexes indicate unambiguously that **4** is a tetravalent terbium complex. The similarity of the multiconfigurational behavior in the ground state of **4** to that observed in TbO_2 further indicates that ligand control of multiconfigurational behavior is a key component of the stability of the complex.

Variable-temperature dc magnetic susceptibility data for **3** and **4** are shown in Fig. 2B. The gradual decrease in the product of the molar magnetic susceptibility and temperature ($\chi_M T$) with decreasing temperature for **3** (orange) corresponds to the gradual depopulation of low-lying crystal field states and is similar in shape and magnitude (room temperature $\chi_M T$ value of 14.2 cm^3 K mol^{-1}) to $\chi_M T$ data observed for Tb^{3+}, $^7F_6$ ions in weak-field complexes.[28, 41] The room temperature $\chi_M T$ value of 8.55 cm^3 K mol^{-1} for **4** (indigo) is consistent with a $^8S_{7/2}$ ion (the theoretical value is 7.94 cm^3 K mol^{-1}), and the field dependent behavior of **4** arises from increased Zeeman splitting at higher fields. Fitting the field dependent behavior of **4** gives a *D* value of 5.5(5) cm^{-1}: an indication of significant zero-field splitting (ZFS) (Fig. S33).

In line with the XAS and susceptibility studies indicating the formation of $^8S_{7/2}$, Kramers ion and, in contrast to Tb^{3+}, **4** presents an X-band EPR spectrum at 12 K in toluene (Fig. 2C). This spectrum diminished at 77 K and completely attenuated at

room temperature indicating a significantly shorter T_1 in comparison to the equivalent trivalent isotropic ion, $^8S_{7/2}$ Gd^{3+}. In the absence of high-frequency and -field EPR (HFEPR) studies [42], a simple model was employed to fit the observed X-band spectrum of **4** using the *D* and *g* values from the magnetic susceptibility fits. The variation of $|E/D|$ (Fig. S34) reveals the transition from an axial spectrum to the principal features of the observed spectrum with the inclusion of rhombic zero-field splitting parameters. This type of EPR spectrum, namely one with significant axial and rhombic zero-field splitting, as opposed to the more isotropic spectrum exhibited by Gd^{3+} species, is indicative of the magnitude of the effective ligand field in tetravalent lanthanides in comparison to trivalent lanthanides.[20, 36-38]

The deep indigo color of **4** in solution is driven by an intense, broad absorption as shown in the UV/vis/NIR spectrum shown in Fig. 2D. The absorption maximum is located at 575 nm with an extinction coefficient of $\varepsilon = 3700\ cm^{-1}\ M^{-1}$ and a full-width at half-maximum peak of 4.28 eV (290 nm). This absorption feature is characteristic of Tb^{4+} and has been previously assigned as a ligand-to-metal charge transfer (LMCT).[15, 30] In complex **4**, the absorption is red-shifted with respect to those observed in oxide coordination environments reflecting the lower ionization potential of N 2p orbitals in comparison to O 2p.[43] Computed UV/vis spectra of **3** and **4** (see Theoretical Calculations section for details) are in excellent agreement with the experimental data (Fig. 2D), confirming the apparent differences in the absorption spectra of **3** and **4**. Specifically, while there is no absorption in the low energy region of **3** (up to 260 nm), theoretical spectrum of **4** exhibits intense electronic excitations in the ~550-775 nm range. According to the natural transition orbital (NTO) analysis, this broad band is attributed exclusively to the excitations originating from the frontier ligand-dominant π molecular orbitals (MOs) (primarily 2p orbitals of N atoms, i.e. from HOMO-18 through HOMO-8, Fig. S36) to the lowest unoccupied MO (LUMO), which is composed of 73% 2p orbitals of N and 27% 6s/4f orbitals of Tb (Fig. S38). Hence, these excitations can be characterized as a dominant ligand-to-ligand charge transfer (LLCT) with an appreciable LMCT contribution. In the higher energy region, this type of excitation emerges up to 320.2 nm. LMCT excitations from the frontier ligand-dominant π MOs to the Tb 4f-dominant LUMOs (N 2p → Tb 4f) emerge in the 217-261 nm range. In contrast to **4**, the N 2p → Tb 4f excitations in **3** do not appear in the considered UV/vis region, and the LLCT bands (N 2p → H 3s) are the major excitations in the 207-260 nm range. The exception is the excitations from HOMO-8 composed of 34% 2p orbitals of N and 66% 6s/4f orbitals of Tb to the ligand-dominant LUMO (93% H 3s) appearing at 224.1 nm (Figs. S37, S39).

The difference in the UV/vis features of **3** and **4** can also be explained by comparing their MO levels (Fig. 3). Since the difference lies in the β MOs, the β electron density is depicted to guide the interpretation of the UV/vis spectra. Upon oxidation, the HOMO level of **3** goes down by 2.37 eV and the occupied HOMO-8 in **3** becomes LUMO in **4**. Due to this, the HOMO-LUMO gap of 5.52 eV in **3** significantly shrinks to 1.28 eV in **4**. Hence, the allowed excitations result in two different energy ranges as observed in the experiment for **3** and **4**. Specifically, these findings support the appearance of the intense excitations corresponding to the broad absorption band in the low-energy region of **4** (575 nm peak maximum) as well as exclusively high-energy excitations occurring in **3** (207-260 nm).

To understand the difference in electronic structure of these complexes, a chemical bonding analysis was developed. Due to the complexity of the canonical MOs, which are intrinsically difficult to interpret in terms of chemical bonds due to delocalization, a Natural Bond Orbital (NBO) analysis was performed. In **3**, there are six one-center, one-electron α NBOs (1c-1e α, or unpaired α electrons) and a lone electron pair (1c-2e NBO) on Tb atom, accounting for a $4f^8$ configuration of **3** (Fig. S41). The six α electrons (Fig. S41A) are pure f-type electrons (99.98% f-character, Table S15) with occupation number (ON) values equal to 1.00 |e|. The lone electron pair on Tb is composed of the 1c-1e α (99.98% *f*-type, ON=1.00 |e|) and 1c-1e β (58% 6*s*/42% 4*f* hybrid, ON=0.96 |e|) NBOs, with overall ON=1.96 |e| (Fig. S41B). Per NBO, the oxidation of **3** occurs due to the removal of this β electron in **3**, resulting in a $4f^7$ ground state electronic configuration of **4** with seven *f*-type 1c-1e α NBOs (Fig. S40). This result further supports the conclusion that the oxidation of **3** is metal-centered.

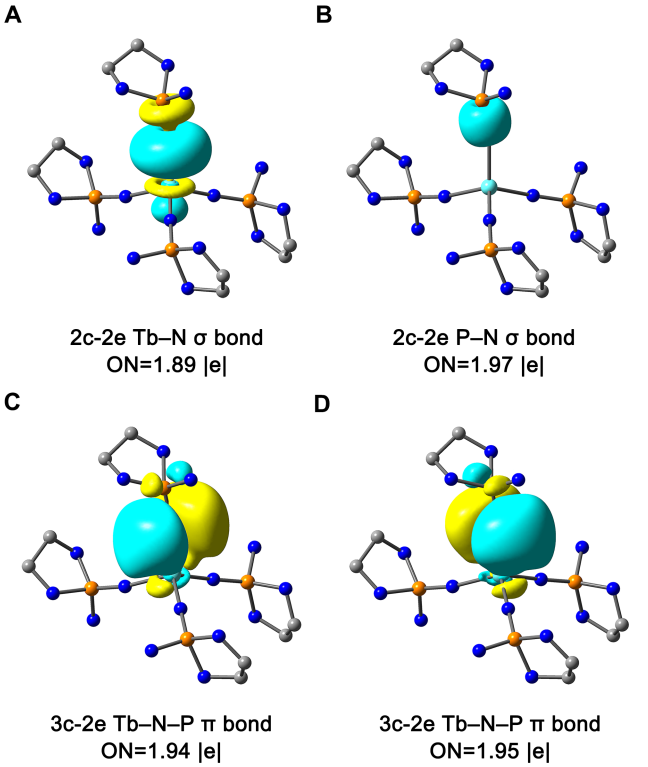

Figure 4. Bonding analysis of the Tb–N–P interactions in **4**. (A) Two-center two-electron Tb–N σ bond. (B) Two-center two-electron P–N σ bond. (C, D) Three-center two-electron Tb–N–P π bonds. ON denotes occupation number. Side groups of the ligands (^{t}Bu, Et_2) are omitted for simplicity. An equivalent set of bonds is identified for other three ligands.

The major bonding interaction between Tb ion and the ligands in **3** occurs due the formation of four two-center two-electron (2c-2e) Tb–N σ bonds with ON=1.96 |e| (Fig. S40A). These bonds are highly polarized towards N atoms (Table S14), accounting for 94.77% of the electron density associated with Tb–N σ bond. While dominant Tb NBO hybrids of the Tb–N σ bonds are composed of *d* (73.49%) and *s* (15.27%) characters, the *f* character is non-negligible, accounting for 10.62% (Table S15). A similar set of Tb–N σ bonds with similar Tb NBO hybrid characters was identified for **4** (Fig. 4). Although the Tb–N σ bonds in **4** exhibit slightly lower ON values of 1.89 |e| (Fig. 4), the polarization towards the N atoms decreases (91.69% for

N), resulting in a more covalent interaction in **4** due to a higher contribution from Tb atoms (0.16 |e| in **4** *vs.* 0.10 |e| in **3** per Tb–N σ bond). These data correlate with the shorter Tb–N bonds in **4** as compared to **3**. Importantly, these findings are in concordance with the previous studies on the Ce^{3+}/Ce^{4+} imidophosphorane complexes,[20] showing a greater covalent character of the M–L bonds in a tetravalent state rather than in the trivalent one.

While the Tb–N σ interactions account for a single bond order between Tb and N in **3** and **4**, there are additional L–M π interactions in both complexes found as two Tb–N–P π bonds per ligand (Fig. 4C, D, S42C, D). In both cases, the eight Tb–N–P π bonds originate from the top eight HOMOs (Figs. S36, 37) with the major contribution coming from N atoms (~93-96% of the electron density per π bond, Table S14). The L–M π donation is found to be larger in **4** (5.69% per Tb–N–P π bond in) than in **3** (2.24%), giving rise to stronger interactions between Tb and N in **4**. In both cases, *d* and *f* characters are dominant in the Tb hybrids of the Tb–N–P π NBOs (Table S15). Since the major contribution to the formation of these bonds comes from N atoms, these 3c-2e π bonds can also be viewed as pure 1c-2e lone electron pairs on N or 2c-2e N–P π bonds, though with lower ON values (Figs. S43-44). The higher ON values of the N–P π bonds in **3** vs. **4** (1.89 |e| vs. 1.82 |e| avg., respectively) support the shorter N–P bond lengths in **3**, confirming the increased electron donation to the metal in **4**. Overall, the NBO results support the greater covalency of the tetravalent *f*-block metal-ligand bonds over the trivalent counterparts, in agreement with previous studies on lanthanide ions.[29, 31, 36-39]

CONCLUSION

The isolation of a molecular tetravalent terbium complex is important for the opportunity to understand the bonding driving the reactivity and magnetic properties of these rare and previously unstable ions in molecular complexes. The broad range of spectroscopic and physical characterization approaches employed in this study move beyond establishing the existence of a new oxidation state and delineate the structural and electronic basis of its stability and its physical properties. The complex design principles presented here provide a road map for the isolation and characterization of reactive tetravalent lanthanide complexes. In particular, the design methodology, which capitalizes on steric and electronic control of imidophosphorane ligand donor properties (orbital energy, orbital radial extent, steric profile, and complex reorganization energy) in a pseudo-tetrahedral environment (S_4), maximizes covalent overlap with both 4*f* and 5*d* orbitals. The increased metal-ligand covalency in the tetravalent oxidation state – as clearly seen in the EPR, XAS, magnetism, and theoretical studies – indicates that significant new applications of tetravalent lanthanide ions in magnetism and chemical reactivity are possible.

EXPERIMENTAL SECTION

General Considerations. Unless otherwise noted, all reagents were obtained from commercial suppliers and the syntheses and manipulations were conducted under argon with exclusion of oxygen and water using Schlenk techniques or in an inert atmosphere box (Vigor) under a dinitrogen (<0.1 ppm O_2/H_2O) atmosphere. The glovebox is equipped with two -35 ˚C freezers. All glassware and cannulae were stored in an oven overnight (>8 h) at a temperature of ca. 160 ˚C. Celite and molecular sieves were dried under vacuum at a temperature >250 ˚C for a minimum of 24 h. C_6D_6 was stored over 3 Å molecular sieves and then vacuum-transferred from purple sodium/benzophenone prior to use. Diethyl ether, *n*-pentane, *n*-hexane, benzene, toluene, tetrahydrofuran, and 1,2-dimethoxyethane were purged with UHP-grade argon (Airgas) and passed through columns containing Q-5 and molecular sieves in a solvent purification system (JC Meyer Solvent Systems). All solvents in the glovebox were stored in bottles over 3 Å molecular sieves. Methanol was dried by refluxing over magnesium turnings activated with iodine for 12 h and then distilled and stored over 3 Å molecular sieves.

The starting materials $TbI_3(THF)_{3.5}$, $[PN(pip)_3]K$, and potassium benzyl were prepared according to literature procedures.[44,20,45] Potassium *t*-butoxide was sublimed prior to use. NMR spectra were obtained on a Bruker Advance III 500 MHz spectrometer at 298 K, unless otherwise noted. ^1H, ^{13}C, and ^{31}P NMR chemical shifts are reported in δ, parts per million. ^1H NMR are referenced to the residual ^1H resonances of the *deutero*-solvent. ^{13}C NMR are referenced to the ^{13}C resonance of the deuterated solvent.[46] Peak position is listed, followed by peak multiplicity, integration value, and proton assignment, where applicable. Multiplicity and shape are indicated by the following abbreviations: s (singlet); d (doublet); t (triplet); q (quartet); dd (doublet of doublets); td (triplet of doublets); m (multiplet); br (broad). Infrared (IR) samples were taken on a Bruker ALPHA FTIR spectrometer from 400 to 4000 cm^{-1}. IR samples were prepared as Nujol mulls sandwiched between two KBr plates. The peaks are listed in wavenumber [cm^{-1}] and intensity using the following abbreviations: vw (very weak); w (weak); m (medium); s (strong); vs (very strong); br (broad). UV/visible/NIR spectroscopy was performed in Teflon-valve sealed quartz cuvettes with a 1 cm path length on a Hitachi UH4150 UV-vis-NIR scanning spectrophotometer between 2400-200 nm. Elemental analyses were determined at Robertson Microlit Laboratories (Ledgewood, NJ).

Crystallographic Analyses. Crystals suitable for X-ray diffraction were covered in paratone oil in a glove box and transferred to the diffractometer in a 20 mL capped vial. Crystals were mounted on a loop with paratone oil on a Bruker D8 VENTURE diffractometer. The crystals were cooled and kept at T = 100(2) K during data collections (except for **3** – see the following description – which was collected at T = 180(2) K). Unless otherwise noted below, the structures were solved with the ShelXT structure solution program using the Intrinsic Phasing solution method and by using Olex2 as the graphical interface.[47, 48] The model was refined with version 2014/7 of XL using Least Squares minimization.[49]

Structure Solution of 3. The crystals of **3** transformed into a multicrystalline form on cooling to 100 K. The transformation occurred at about 150 K. The data set that was collected at 100 K (**3–100K**) was comprised of reflections from a polycrystalline sample, but a significant portion (>25%) the diffraction data was from a single crystal of this compound. The data was of high enough quality for a structure solution and refinements. The phase change was accompanied by a lowering of the symmetry of the structure. The forbidden reflections h+k=2n associated with the C-centering were strongly observed. Thus, the space group symmetry decreased from C2/c to P2(1)/n (a non-conventional space group was adopted to preserve the same cell axes). The Tb structure at 180 K has the C-centered lattice and the Tb and K atoms on special positions (sites of 2-fold symmetry) with half the atoms generated by crystallographic symmetry. Interestingly, on cooling to 100 K the site symmetry of the Tb atom is reduced and the coordination geometry becomes less regular with 4 different Tb–N bond lengths instead of 2 different bond lengths. The lower symmetry structure **3–100K** is included in the SI for comparison.

Structure solution of 4. The structure would not solve using the standard structure solution programs. The crystal was not obviously twinned and all the reflections appeared to be single. Close inspection of the data in XPREP showed that the data appeared to have Laue symmetry 4/mmm but true Laue symmetry 4/m.[50] Thus the crystal is a merohedral twin with the twin law being a two-fold axis along the crystallographic direction [110]. The structure was partially solved in the space group I-4 (# 82) by the ShelXT structure solution program on detwinned data (from XPREP) using the Dual Space Method.[47] The structure was refined as 4-component twin that combined the merohedral twinning with inversion twinning (the twin also appears to be a mirror along [110]) and refined by Least Squares using version 2018/3 of ShelXL.[49] All non-hydrogen atoms were refined anisotropically. Hydrogen atom positions were calculated geometrically and refined using the riding model.

EPR. X-band EPR measurements were performed on a Bruker ESP-300 with an Oxford ESR-900 cryostat and Oxford temperature controller at 9.3640 GHz on a sample of **4** at 12, 30, and 50 K and on a modified Varian E-9 spectrometer at 77 K (L N_2 finger dewar) and at room temperature. The liquid helium measurements were performed in both toluene and toluene/THF (1:1 v/v). No difference was seen in the spectra between the two solvent systems. EPR simulations used the program SPIN (A. Ozarowski, NHMFL).

Magnetism. Magnetic measurements were performed on a Quantum Design MPMS-5S magnetometer. Inside of a glovebox, a measured amount of quartz wool (10-20 mg) was loaded and packed tightly into a quartz tube. Powdered samples were loaded inside of the tube and onto the glass wool plug by tapping the compound through a glass pipet. Another pre-massed amount of quartz wool (10-20 mg) was loaded on top of the sample and contents packed tightly again. The top of the tube was affixed to an Ultra Torr Swagelok adaptor while the bottom was plugged with a piece of snug tubing tightly closed with a stopper and copper wire. This was transported from the glovebox to a Schlenk line where it was sealed above and below the sample using a O_2/H_2 torch while the sample was under vacuum. The vacuum sealed tubing was taped to a straw and the straw was loaded into the instrument. Diamagnetic corrections for the quartz wool and the ligand were performed using Pascal's constants.[51] Ferromagnetic corrections for residual iron in samples was performed according to published procedure.[52]

Tb L_3-edge Measurements. Terbium samples were prepared in an argon glovebox at SSRL since both Tb^{4+} and Tb^{3+} complexes are air-sensitive. A mixture of the analyte and boron nitride (BN) was weighed, such that the edge jump for the absorbing atom was calculated to be at one absorption length in transmission (~8-12 mg for Tb samples). The samples were diluted with BN (~10 mg) that had been dried at elevated temperature (250 °C) under vacuum (1×10^{-3} Torr) for 24 h prior to use. Samples were ground with a mortar and pestle.

Solid-state sample holders for the Tb samples consisted of an aluminum plate with a 3 × 15 mm oval window and screw holes. One side of the plate was covered with 0.5 mm Kapton tape, and the sample was evenly loaded in the window. The powder was then secured by covering the sample with a second piece of 0.5 mm Kapton tape. A second layer of compound was painted onto a third piece of Kapton tape, which was subsequently fixed to the backside of the sample holder. The sample holder was then loaded onto a sample rod, taken out of the glovebox, and transported to the beamline while submerged within a $N_{2(liq)}$ cooling bath. Once at the beam, the rod with the sample was placed at 45° inside the Oxford $He_{(liq)}$ cryostat, which was precooled at 85 K and attached to the SSRL Beamline 11-2 rail. When the cryostat was closed, the system was put under vacuum and flushed with helium five times. The valve was closed, and the measurements were performed in the cryostat at 10 K.

The solid-state terbium complexes were characterized by metal L_3-edge X-ray measurements. The X-ray absorption measurements were made at SSRL, under dedicated operating conditions (3.0 GeV, 5%, 500 mA using continuous top-off injections) on end station 11-2. With the use of a liquid nitrogen-cooled double-crystal Si(220) (φ=0) monochromator that employed collimating and focusing mirrors, a single energy was selected from the incident white beam. For Tb measurements, the beam was fully tuned at 7514 eV and harmonic rejection was achieved with a manganese foil. The horizontal slit sizes were 10 mm and vertical slit sizes were 1 mm in all measurements.

The cryostat was attached to the beamline 11-2 XAS rail (SSRL), which was equipped with three ionization chambers, through which nitrogen gas was continually flowed. One chamber was positioned before the helium beam pass and the cryostat (10 cm) to monitor the incident radiation (I_0). The second chamber was positioned after the cryostat (30 cm) so that sample transmission (I_1) could be evaluated against I_0 and so that the absorption coefficient (μ) could be calculated as $\ln(I_0/I_1)$. The third chamber (I_2; 30 cm) was positioned downstream from I_1 so that the XANES of a calibration foil could be measured against I_1. A potential of 1100 V was applied in series to the ionization chambers. A PIPS detector under argon was placed on one side of the cryostat (4 cm) to detect the fluorescence from the samples. The Tb samples were calibrated in situ to the energy of the first inflection point of the K-edge of iron foil (7112 eV). Data were acquired in triplicate and averaged. Background subtraction and normalization (at 7514 eV) were performed in Athena.

Curve-fitting was performed in IgorPro 7.0 using a modified version of EDG_FIT.[53] Derivative spectra were used as guides to determine the number and position of peaks, and edge features were modeled by Voigt line shapes and an additional function consisting of arctangent and error function contributions, which was used to model the absorption threshold. Deconvoluted spectral models were performed over several energy ranges. In the spectrum of **4**, 3 Voigts were employed to fit the spectrum: p_1 (the quadrupole allowed $2p_{3/2}\rightarrow 4f$ transition), p_2 and p_3 to model the double-white line feature. In the spectrum of **3** a single Voigt was employed to model the white-line feature. The area under the Voigt functions (defined as the intensity) was calculated with the formula $\mathrm{ph}\times\mathrm{fwhm}\times1/4\times([\pi/\ln(2)]^{1/2}+\pi)$, where ph = peak height (normalized intensity), fwhm = full-width at half-maximum height (eV), and the value $1/4\times([\pi/\ln(2)]^{1/2}+\pi)\approx 1.318$ is a constant associated with the Voigt function. The fits are shown in Fig. S45 and summarized in Table S17. Relative parameter error estimates are calculated from the covariance matrix assuming normally distributed variances in the data. Absolute error in n_f is about 0.04 or 10%.

Theoretical Calculations. All the calculations were carried out with the PBE0[54] hybrid functional as implemented in the Gaussian 09 software package revision C.01.[55] ECP28MWB[56] small core quasi-relativistic pseudopotential and ECP28MWB_ANO[57] basis set were used to describe Tb, and the remaining atoms were described with the all-electron Pople basis set 6-311G(d).[57] The geometries of compounds **3** (excluding the $K(Et_2O)^+$ counter ion fragment) and **4** were optimized in gas phase without any constraints. Harmonic frequency calculations were performed to confirm that the optimized structures were stationary points on the potential energy surface. The computed structural metrics are in good agreement with the XRD data, with Tb−N and N−P bond distances, as well as Tb−N−P valence angles within 3.9%, 0.4%, and 3.3% of the experimental ones, respectively, providing confidence to the theoretical model (Table S13). In all calculations, spin contamination was found to be less than 5.2% with $\langle S^2\rangle$ values being close to the corresponding values of the considered spin states, i.e. septet for **3** (C_2 point group symmetry) and octet for **4** (S_4 point group symmetry). Wavefunctions of the studied species were found to be stable indicating that the calculations converged to the ground electronic state. Time-dependent DFT calculations (TD-DFT) of up to 200 excited states were carried out to simulate the experimental UV-Vis spectrum of both complexes. The computed UV-Vis spectra were plotted broadening the calculated excitation lines with Gaussian-type peaks using 0.05 eV half-width at half height. Natural transition orbitals (NTOs),[58] which most of the time can yield a single electron-hole representations of the electronic excitations, were employed to interpret the calculated excitation spectra. To gain more insight into electronic structure of these complexes, chemical bonding analyses were performed using Natural Bond Orbital[59, 60] (NBO6) method. The GaussView 6[61] was used for molecular orbitals visualization of the NBO results. Chemissian 4.60[62] was used to plot molecular orbital energy level diagrams.

Syntheses. A scheme providing an overview for all syntheses is provided in Figure S1.

N,N'-di-*tert*-butylethylenediamine, 5. Synthesis of **5** was modified from a previous report.[63] In air, 1,2-dibromoethane (86 mL, 1 mol) and 350 mL of water were added to a 2 L round bottom flask equipped with a Teflon stir bar. The reaction mixture was chilled to 0 °C, and *tert*-butylamine (526 mL, 5 mol) was added dropwise to the solution. The reaction mixture was kept in an ice bath for 1 h and then stirred at 25 °C for 4 d. Solid NaOH was added in 25 g portions until it no longer dissolved (no change over 3 h). The biphasic mixture was then decanted and stirred over an additional 25 g of ground NaOH for 30 h. The top layer was then obtained via separatory funnel and the liquid was filtered into a 250 mL Schlenk round bottom flask. Pre-sliced pieces of Na metal were added (~ 4 g) and the mixture was distilled at 66 – 69 °C at ~30 torr to yield a clear, colorless liquid (97.13 g, 56%). ^{1}H NMR (400 MHz, C_6D_6): 2.67 (4H, s, (CH_2N^tBu)), 1.12 (18H, s, (CH_2N^tBu)).

[$(CH_2N^tBu)_2PCl$], 6. Synthesis of **6** was modified from a previous report.[64] PCl_3 (6 mL, 68.6 mmol) was added to a 500 mL Schlenk round bottom flask containing 350 mL diethyl ether and a Teflon stir bar. The reaction mixture was cooled to -20 °C and triethylamine (50 mL, 360

mmol) was added to the reaction mixture and, subsequently, **5** (15 mL, 69.6 mmol) was added dropwise over 15 min. A thick, white precipitate quickly formed. The reaction mixture was stirred for 6 h at 25 °C and then transferred to the glovebox where it was filtered through a medium porosity frit packed with Celite and washed twice with 30 mL diethyl ether to yield a clear, colorless filtrate. The solution was concentrated *in vacuo* and placed inside a -35 °C freezer overnight. Colorless, needle-like crystals were isolated by decantation and the remaining volatiles removed *in vacuo* to afford 6 (11.677 g, 72%). ^{1}H NMR (500.3 MHz, C_6D_6): 3.07 (2H, m, (CH_2N^{t}Bu)), 2.79 (2H, m, (CH_2N^{t}Bu)), 1.24 (18H, d, J = 2.1 Hz, NC(CH_3)$_3$).^{13}C NMR (125.8 MHz, C_6D_6): 53.2 (d, $^2J_{CP}$ = 10.9 Hz, NC(CH_3)), 44.9 (d, $^2J_{CP}$ = 10.5 Hz, CH$_2$N^{t}Bu), 28.4 (d, $^3J_{CP}$ = 11.9 Hz, NC(CH_3)$_3$). ^{31}P NMR (202.5 MHz, C_6D_6): 157 (s). IR: ν [cm^{-1}] = 1396 (w), 1376 (m), 1363 (m), 1268 (w), 1256 (w), 1244 (w), 1221 (s), 1208 (s), 1128 (m), 1120 (m), 1088 (w), 1040 (m), 1026 (w), 982 (m), 863 (w), 802 (w), 676 (w), 665 (w). Elemental analysis found(calculated): C, 50.98(50.74), H, 9.38(9.37), N, 11.97(11.83).

[P(1,2-*bis*-^{t}Bu-diamidoethane)(NEt$_2$)], 7. Inside a glovebox, **6** (11.59 g, 49 mmol) was added to a 500 mL Schlenk round bottom flask equipped with a Teflon stir bar and dissolved in 200 mL of diethyl ether. The flask was transferred to the Schlenk line and cooled to 0 °C. Diethylamine (20 mL, 196 mmol) was added dropwise to the solution over 5 min. A thick, white precipitate quickly formed. The reaction mixture was stirred for 20 h at 25 °C and then transferred to the glovebox where it was filtered through a medium porosity frit packed with Celite and washed with two times with 15 mL of diethyl ether to yield a clear, colorless filtrate. Volatiles were removed *in vacuo* to yield a clear, colorless, viscous liquid. The liquid was distilled at 55 – 58 °C at ~170 mtorr to afford the title compound as a clear, colorless liquid (12.52 g, 93%). ^{1}H NMR (500 MHz, C_6D_6): 3.17 (2H, m, CH_2N^{t}Bu), 3.06 (4H, p, J = 7.1 Hz, NCH_2CH$_3$), 2.86 (2H, m, CH_2N^{t}Bu), 1.29 (18H, s, NC(CH_3)$_3$), 1.07 (6H, t, J = 7.1 Hz, NCH$_2$CH_3). ^{13}C NMR (MHz, C_6D_6): 52.4 (d, J = 17.9 Hz), 45.4 (d, J = 8.2 Hz), 40.3 (d, J = 20.2 Hz), 29.5 (d, J = 10.2 Hz), 14.9 (d, J = 3.1 Hz). ^{31}P{^{1}H} NMR (MHz, C_6D_6): 101 (s). IR: ν [cm^{-1}] = 1458 (w), 1387 (m), 1369 (w), 1358 (m), 1340 (w), 1288 (w), 1261 (m), 1242 (m), 1219 (m), 1195 (m), 1133 (m), 1094 (w), 1052 (w), 1031 (w), 1014 (m), 965 (m), 906 (m), 865 (m), 787 (m), 668 (m), 632 (w). Elemental analysis found(calculated): C, 61.26(61.50), H, 11.50(11.80), N, 14.64(15.37).

[HN=P(1,2-*bis*-^{t}Bu-diamidoethane)(NEt$_2$)], 8. The title compound was prepared through a one flask, two-step reaction sequence. Inside a glove box, **7** (4.058 g, 15 mmol) was dissolved in 25 mL of toluene inside a 100 mL Schlenk pear flask equipped with a Teflon stir bar. Trimethylsilylazide (32 mmol) was added to the flask and the flask was transferred to the Schlenk line. The reaction mixture was refluxed for 3 d. Volatiles were removed *in vacuo* to yield a yellow residue. Dry, degassed methanol (24 mL, 596 mmol) and 2 drops of 96% H_2SO_4 were added. The yellow solution was stirred at 25 °C for 2 d. Volatiles were removed *in vacuo* to yield a viscous, turbid, yellow liquid. The liquid was transferred to a 50 mL Schlenk round bottom flask and distilled at 75 – 78 °C at 60 mtorr to yield the product as a viscous, clear, colorless liquid (1.94 g, 45%). ^{1}H NMR (500 MHz, C_6D_6): 3.18 (4H, dq, J = 10.2, 7.1 Hz, NCH_2CH$_3$), 2.71 (4H, m, (CH_2N^{t}Bu)$_2$), 1.29 (18H, s, (NC(CH_3)$_3$)$_2$), 1.09 (6H, t, J = 7.1 Hz, NCH$_2$CH_3), 0.37 (1H, br s, P=N-H). ^{13}C{^{1}H} NMR (500 MHz, C_6D_6): 52.6 (d, J = 5.4 Hz, NC(CH_3)$_3$), 40.7 (d, J = 10.8 Hz, CH$_2$N^{t}Bu), 40.4 (d, J = 4.6 Hz, NCH_2CH$_3$), 28.6 (d, J = 3.1 Hz, NC(CH_3)$_3$), 14.1 (d, J = 2.7 Hz, NCH$_2$$CH_3$). ^{31}P{^{1}H} NMR (500 MHz, C_6D_6): 30.7 (s). IR: ν [cm^{-1}] = 3389 (m), 1479 (m), 1465 (m), 1391 (s), 1378 (s), 1361 (s), 1268 (s), 1248 (s), 1225 (s), 1208 (s), 1192 (s), 1150 (s), 1108 (s), 1091 (w), 1052 (s), 1035 (s), 1019 (w), 979 (s), 944 (s), 869 (s), 800 (m), 789 (w), 693 (m), 645 (m), 617 (w). Elemental analysis of the air-sensitive liquid was not performed. The =NTMS intermediate, [TMSN=P(1,2-*bis*-^{t}Bu-diamidoethane)(NEt$_2$)], can be isolated, if desired, prior to the addition of methanol and sulfuric acid through removal of volatiles *in vacuo* and crystallization from hexanes at -35 °C. ^{1}H NMR (500 MHz, C_6D_6): 2.99 (4H, dq, J = 11.1, 7.2 Hz, NCH$_2$CH$_3$), 2.76 (2H, m, CH$_2$N^{t}Bu), 2.64 (2H, m, CH$_2$N^{t}Bu), 1.25 (18H, s, NC(CH_3)$_3$), 1.04 (6H, t, J = 7.2 Hz), 0.44 (9H, s, =N-Si(CH_3)$_3$). ^{13}C{^{1}H} NMR (500 MHz, C_6D_6): 52.4 (d, J = 4.7 Hz, NC(CH_3)$_3$), 40.9 (d, J = 6.4 Hz, CH$_2$N^{t}Bu), 40.4 (d, J = 12.6 Hz, NCH$_2$CH$_3$),14.2 (d, J = 3.0 Hz, NCH$_2$CH$_3$), 4.63 (d, J = 2.5 Hz, =N-Si(CH_3)$_3$). ^{31}P{^{1}H} NMR (500 MHz, C_6D_6): -0.25 (s). Elemental analysis found(calculated): C, 56.81(56.62), H, 11.34(11.46), N, 15.55(15.54).

[(CH$_2$N^{t}Bu)$_2$(Et$_2$N)P=NK], 2. Inside a glovebox, **8** (1.273 g, 4.413 mmol) was added to a 20 mL scintillation vial equipped with a Teflon stir bar and dissolved in 4 mL of hexanes. Potassium benzyl (0.576 g, 4.420 mmol) was added as a solid. Any remaining potassium benzyl was slurried in a small amount (~ 2 mL) of hexanes and added to the reaction mixture. The orange slurry was stirred for 1 h then filtered through a fine porosity frit packed with Celite. The orange solution was concentrated *in vacuo* and placed inside a -35 °C freezer overnight during which colorless crystals formed. The crystals were isolated by decantation and recrystallized from diethyl ether at -35 °C overnight to yield **2** as clear, colorless, XRD quality crystals (1.3534 g, 93%). ^{1}H NMR (500.3 MHz, C_6D_6): 2.99-2.97 (4H, m, NCH_2CH$_3$), 3.25-3.20 (4H, m, (CH_2N^{t}Bu)$_2$), 1.42 (18H, s, (NC(CH_3)$_3$)$_2$), 1.21 (6H, t, J = 7.1 Hz, NCH$_2$CH_3). ^{13}C{^{1}H} NMR (500 MHz, C_6D_6): 51.37 (d, J = 4.9 Hz, NC(CH_3)$_3$), 41.81 (d, J = 2.4 Hz, CH$_2$N^{t}Bu), 41.69 (d, J = 6.9 Hz, NCH_2CH$_3$), 29.72 (d, J = 2.1 Hz, NC(CH_3)$_3$), 15.55 (d, J = 3.1 Hz, NCH$_2$$CH_3$). ^{31}P{^{1}H} NMR (500 MHz, C_6D_6): -10.48 (s). IR: ν [cm^{-1}] = 2041 (w), 1354 (m), 1346 (m), 1266 (m), 1249 (m), 1226 (m), 1202 (s), 1182 (m), 1146 (m), 1094 (w), 1050 (m), 1020 (m), 967 (m), 946 (w), 908 (m) 788 (m), 674 (m), 611 (m). Elemental analysis found(calculated): C, 51.14(51.50), H, 9.77(9.88), N, 16.95(17.16).

[(Et$_2$O)KTb((pip)$_3$PN)$_4$], 1. Inside a glovebox, TbI$_3$(THF)$_{3.5}$ (0.170 g, 0.214 mmol) was added to a 20 mL scintillation vial charged with a stir bar and 1 mL THF. [PN(pip)$_3$]K (0.300 g, 0.868 mmol), was added as a solution in THF (4 mL) and the reaction mixture was stirred overnight. The mixture was filtered through a fine porosity frit packed with Celite. The filtrate was concentrated *in vacuo* to give an off white solid. The residue was triturated five times with 1 mL *n*-pentane and then taken up in 3 mL diethyl ether and filtered through a pipet filter packed with Celite and glass filter paper. The pale, yellow solution was concentrated *in vacuo* and placed inside a -35° C freezer overnight during which a white solid precipitated from solution. Isolation of the precipitate by decantation and removal of residual volatiles *in vacuo* afforded the title compound (43 %, 0.1278 g). ^{1}H NMR (400 MHz, C_6D_6): -7.08-7.43 (m 72 H), -29.20 (s, 48 H, fwhm: 538 Hz). No ^{13}C, or ^{31}P NMR signal were observed. IR: ν [cm^{-1}] = 1451 (s), 1440 (s), 1323 (s), 1273 (w), 1256 (m), 1249 (m), 1198 (s), 1159 (s), 1125 (s), 1110 (m), 1057 (s), 1028 (s), 948 (s), 935 (s), 853 (m), 834 (m), 810 (w), 705 (s), 666 (w), 563 (w). Elemental analysis found(calculated): C, 50.39(51.93), H, 9.16(8.72), N, 15.68(16.15). Carbon was consistently low on multiple burns. XRD quality crystals were grown from evaporation of diethyl ether at -35 °C.

[(Et$_2$O)K][Tb(NP(1,2-*bis*-^{t}Bu-diamidoethane)(NEt$_2$))$_4$], (3). Inside a glovebox, TbI$_3$(THF)$_{3.5}$ (0.182 g, 0.230 mmol) was added to a 20 mL scintillation vial charged with a stir bar and 2 mL diethyl ether. **2** (0.300 g, 0.919 mmol) was added as a solution in diethyl ether (3 mL) and the reaction mixture was stirred overnight. The mixture was filtered through a fine porosity frit packed with Celite. The filtrate was concentrated *in vacuo* to give a colorless solid. The residue was triturated five times with 1 mL *n*-pentane and then taken up in 3 mL hexanes and filtered through a pipet filter packed with Celite and glass fiber filter paper. The pale-yellow solution was concentrated *in vacuo* and placed into a -35° C freezer. Overnight colorless crystals formed which were isolated by decantation and residual volatiles were removed *in vacuo* to afford the title compound (55%, 0.197 g). Only 3 of the 4 expected resonances are observed. ^{1}H NMR (400 MHz, C_6D_6): 28.00 (s, fwhm: 99 Hz), 10.57 (s, fwhm: 65 Hz), 4.72 (s, fwhm: 224 Hz). No ^{13}C, or ^{31}P NMR signals were observed. IR: ν [cm^{-1}] = 1356(m), 1267 (m), 1250 (m), 1210 (m), 1196 (m), 1170 (s), 1150 (m), 1094 (w), 1056 (m), 1029 (m), 975 (m), 927 (m), 916 (w), 868 (m), 795 (m), 691 (m), 627 (w). Elemental analysis found(calculated): C, 49.44(49.91), H, 9.36(9.57), N, 16.29(16.63). XRD quality crystals were grown from diethyl ether at -35 °C.

[Tb(NP(1,2-*bis*-^{t}Bu-diamidoethane)(NEt$_2$))$_4$], 4. Inside a glovebox, **3** (0.1771 g, 0.13 mmol) was dissolved in 2 mL diethyl ether in a 20 mL scintillation vial charged with a stir bar. AgI (0.034 g, 0.15 mmol) was added to the scintillation vial as a suspension in diethyl

ether (3 mL). Upon addition, the clear, colorless solution turned a deep indigo and the reaction mixture was stirred for 5 min. A fine grey powder and a white precipitate were formed during the course of the reaction. The mixture was filtered through a pipet filter packed with Celite and glass fiber filter paper and then volatiles were removed *in vacuo*. The residue was triturated 5 times with 1 mL *n*-pentane. The residue was then taken up in diethyl ether, filtered through a pipet filter packed with Celite and glass fiber filter paper, concentrated *in vacuo*, and placed into a -35 °C freezer. Overnight indigo crystals formed which were isolated by decantation and residual volatiles were removed *in vacuo* to afford the title compound (55%, 0.094 g). No ^{1}H or ^{31}P NMR signals were observed. IR: ν [cm^{-1}] = 1358 (m), 1268 (m), 1251 (m), 1227 (w), 1211 (m), 1195 (m), 1152 (w), 1112 (s), 1074 (w), 1059 (m), 1050 (w), 1026 (m), 980 (m), 935 (m), 921 (w), 871 (w), 799 (m), 703 (m), 636 (w). Elemental analysis found(calculated): C, 48.68(51.40), H, 9.98(9.86), N, 16.33(17.13). Carbon was consistently low on multiple burns. XRD quality crystals were grown from *n*-pentane at -35 °C.

ASSOCIATED CONTENT

Supporting Information

The Supporting Information is available free of charge on the ACS Publications website at DOI: [to be inserted later].

Complete experimental details, NMR and UV−vis spectra, computational details including Cartesian coordinates, magnetism data, XANES fitting details, and crystallographic data (PDF). Crystallographic data for **1**, **2**, **3**, **3−100K**, and **4** (CIF).

Accession Codes

CCDC 1910602, 1910318, 1910600, 1915172, and 1910601 contain the supplementary crystallographic data for this paper. These data can be obtained free of charge via www.ccdc.cam.ac.uk/data_request/cif, or by emailing data_request@ccdc.cam.ac.uk, or by contacting The Cambridge Crystallographic Data Centre, 12 Union Road, Cambridge CB2 1EZ, UK; fax: +44 1223 336033.

AUTHOR INFORMATION

Corresponding Author

* Henry S. La Pierre: hsl@gatech.edu

ORCID

Natalie T. Rice: 0000-0002-6233-7958
Ivan A. Popov: 0000-0003-2663-3685
Dominic R. Russo: 0000-0003-4014-9216
Joshua Telser: 0000-0003-3307-2556
Ping Yang: 0000-0003-4726-2860
Enrique R. Batista: 0000-0002-3074-4022
Henry S. La Pierre: 0000-0002-0895-0655

Notes

The authors declare no competing financial interest.

ACKNOWLEDGMENT

This material is based upon work supported by Georgia Institute of Technology and the U.S. Department of Energy, Office of Science, Office of Basic Energy Sciences, Heavy Element Chemistry Program under Award Number DE-SC0019385. Single-crystal diffraction experiments were performed at the GT SC-XRD facility directed by J.B. Prof. Brian M. Hoffman, Northwestern University, provided access to EPR spectrometers, which are supported by NSF (MCB-1118613). Use of the Stanford Synchrotron Radiation Lightsource, SLAC National Accelerator Laboratory, is supported by the U.S. Department of Energy, Office of Science, Office of Basic Energy Sciences under Contract No. DE-AC02-76SF00515. The SSRL Structural Molecular Biology Program is supported by the DOE Office of Biological and Environmental Research, and by the National Institutes of Health, National Institute of General Medical Sciences (including P41GM103393). I.A.P. is supported by a J. Robert Oppenheimer Distinguished Postdoctoral Fellowship at Los Alamos National Laboratory. E.R.B. and P.Y. are supported by the Heavy Element Chemistry Program sponsored by the Division of Chemical Sciences, Geosciences, and Biosciences, Office of Basic Energy Sciences, U.S. Department of Energy, at Los Alamos National Laboratory (LANL). LANL is operated by Triad National Security, LLC, for the National Nuclear Security Administration of U.S. Department of Energy (Contract No. 89233218CNA000001).

REFERENCES

1. Cotton, F. A.; Wilkinson, G.; Murillo, C. A.; Bochmann, M., The Group 3 Elements and the Lanthanides. In *Advanced Inorganic Chemistry, 6th Edition*, Wiley-Interscience: New York, 1999; pp 1108-1129.
2. L. Arnold, P.; Geoffrey N. Cloke, F.; B. Hitchcock, P., The first structurally authenticated zerovalent heteroarene complex of a lanthanide; synthesis and X-ray structure of bis(2,4,6-tri-tert-butyl- phosphorin)holmium(O). *Chemical Communications* **1997,** (5), 481-482.
3. B., H. P.; F., L. M.; Laurent, M.; V., P. A., Lanthanum Does Form Stable Molecular Compounds in the +2 Oxidation State. *Angewandte Chemie International Edition* **2008,** *47* (8), 1488-1491.
4. MacDonald, M. R.; Bates, J. E.; Fieser, M. E.; Ziller, J. W.; Furche, F.; Evans, W. J., Expanding Rare-Earth Oxidation State Chemistry to Molecular Complexes of Holmium(II) and Erbium(II). *Journal of the American Chemical Society* **2012,** *134* (20), 8420-8423.
5. Fieser, M. E.; Ferrier, M. G.; Su, J.; Batista, E.; Cary, S. K.; Engle, J. W.; Evans, W. J.; Lezama Pacheco, J. S.; Kozimor, S. A.; Olson, A. C.; Ryan, A. J.; Stein, B. W.; Wagner, G. L.; Woen, D. H.; Vitova, T.; Yang, P., Evaluating the electronic structure of formal Ln^{II} ions in $Ln^{II}(C_5H_4SiMe_3)_3^{1-}$ using XANES spectroscopy and DFT calculations. *Chemical Science* **2017,** *8* (9), 6076-6091.
6. Fieser, M. E.; Palumbo, C. T.; La Pierre, H. S.; Halter, D. P.; Voora, V. K.; Ziller, J. W.; Furche, F.; Meyer, K.; Evans, W. J., Comparisons of lanthanide/actinide +2 ions in a tris(aryloxide)arene coordination environment. *Chemical Science* **2017,** *8* (11), 7424-7433.
7. During the preparation of this Article, a related example of a tetravalent terbium complex was reported. See reference 8.
8. Palumbo, C. T.; Zivkovic, I.; Scopelliti, R.; Mazzanti, M., A Molecular Complex of Tb in the +4 Oxidation State. *Journal of the American Chemical Society* **2019**, *ASAP*, DOI: 10.1021/jacs.9b05337.
9. The core data in this Article was presented at an ACS National Meeting prior to publication and prior to submission of reference 8. See references 10 and 11.
10. Rice, N. T.; Su, J.; Batista, E. R.; Bacsa, J.; Yang, P.; La Pierre, H. S. *Homoleptic imidophosphorane cerium complexes: Potent thermodynamic reductants and stabilization of tetravalent oxidation state*, 257th ACS National Meeting & Exposition, Orlando, FL, March 31st, 2019; INOR-0069.
11. La Pierre, H. S.; Su, J.; Rice, N. T.; Gompa, T. P.; Russo, D. R.; Aguirre-Quintana, L. M.; Bacsa, J.; Batista, E. R.; Yang, P. *Perturbing the balance between ionic and covalent bonding in early actinide complexes*, 257th ACS National Meeting & Exposition, Orlando, FL, April 4th, 2019; INOR-1027.
12. Cheisson, T.; Schelter, E. J., Rare earth elements: Mendeleev's bane, modern marvels. *Science* **2019,** *363* (6426), 489-493.
13. Nash, K. L., A Review of the Basic Chemistry and Recent Developments in Trivalent f-Elements Separations. *Solvent Extraction and Ion Exchange* **1993,** *11* (4), 729-768.

14. Nugent, L. J.; Baybarz, R. D.; Burnett, J. L.; Ryan, J. L., Electron-transfer and f-d absorption bands of some lanthanide and actinide complexes and the standard (II-III) oxidation potential for each member of the lanthanide and actinide series. *The Journal of Physical Chemistry* **1973,** *77* (12), 1528-1539.
15. Hobart, D. E.; Samhoun, K.; Young, J. P.; Norvell, V. E.; Mamantov, G.; Peterson, J. R., Stabilization of Praseodymium(IV) and Terbium(IV) in Aqueous Carbonate Solution. *Inorg. Nucl. Chem. Letters* **1980,** *16*, 321-328.
16. Varlashkin, P. G.; Begun, G. M.; Peterson, J. R., On the Nature of Tetravalent Terbium in Carbonate-Hydroxide Solutions. *Journal Less-Common Metals* **1985,** *109*, 123-134.
17. Li, X.; Dong, W.; Qi, Y.; Wang, D.; Yang, R., Studies on the Stabilization of Terbium(IV) in Aqueous Tetrametaphophate Solution. *Polyhedron* **1991,** *10* (13), 1479-1483.
18. Piro, N. A.; Robinson, J. R.; Walsh, P. J.; Schelter, E. J., The electrochemical behavior of cerium(III/IV) complexes: Thermodynamics, kinetics and applications in synthesis. *Coordination Chemistry Reviews* **2014,** *260*, 21-36.
19. Levin, J. R.; Dorfner, W. L.; Carroll, P. J.; Schelter, E. J., Control of cerium oxidation state through metal complex secondary structures. *Chemical Science* **2015,** *6* (12), 6925-6934.
20. Rice, N. T.; Su, J.; Gompa, T. P.; Russo, D. R.; Telser, J.; Palatinus, L.; Bacsa, J.; Yang, P.; Batista, E. R.; La Pierre, H. S., Homoleptic Imidophosphorane Stabilization of Tetravalent Cerium. *Inorganic Chemistry* **2019,** *58* (8), 5289-5304.
21. Shannon, R., Revised effective ionic radii and systematic studies of interatomic distances in halides and chalcogenides. *Acta Crystallographica Section A* **1976,** *32* (5), 751-767.
22. Robinson, J. R.; Carroll, P. J.; Walsh, P. J.; Schelter, E. J., The Impact of Ligand Reorganization on Cerium(III) Oxidation Chemistry. *Angewandte Chemie International Edition* **2012,** *51* (40), 10159-10163.
23. Anwander, R.; Dolg, M.; Edelmann, F. T., The difficult search for organocerium(IV) compounds. *Chemical Society Reviews* **2017,** *46* (22), 6697-6709.
24. Pham, T. A.; Altman, A. B.; Stieber, S. C. E.; Booth, C. H.; Kozimor, S. A.; Lukens, W. W.; Olive, D. T.; Tyliszczak, T.; Wang, J.; Minasian, S. G.; Raymond, K. N., A Macrocyclic Chelator That Selectively Binds Ln^{4+} over Ln^{3+} by a Factor of 1029. *Inorganic Chemistry* **2016,** *55* (20), 9989-10002.
25. Deblonde, G. J. P.; Sturzbecher-Hoehne, M.; Rupert, P. B.; An, D. D.; Illy, M.-C.; Ralston, C. Y.; Brabec, J.; de Jong, W. A.; Strong, R. K.; Abergel, R. J., Chelation and stabilization of berkelium in oxidation state +IV. *Nature Chemistry* **2017,** *9*, 843.
26. Noh, W.; Girolami, G. S., X-ray crystal structure of the tetra(tert-butyl)erbate anion and attempts to prepare tetravalent organolanthanide complexes. *Polyhedron* **2007,** *26* (14), 3865-3870.
27. Kim, J. E.; Bogart, J. A.; Carroll, P. J.; Schelter, E. J., Rare Earth Metal Complexes of Bidentate Nitroxide Ligands: Synthesis and Electrochemistry. *Inorganic Chemistry* **2016,** *55* (2), 775-784.
28. Gregson, M.; Lu, E.; Mills, D. P.; Tuna, F.; McInnes, E. J. L.; Hennig, C.; Scheinost, A. C.; McMaster, J.; Lewis, W.; Blake, A. J.; Kerridge, A.; Liddle, S. T., The inverse-trans-influence in tetravalent lanthanide and actinide bis(carbene) complexes. *Nature Communications* **2017,** *8*, 14137.
29. Baker, J. M.; Chadwick, J. R.; Garton, G.; Hurrell, J. P., E.P.R. and ENDOR of Tb^{4+} in Thoria. *Proceedings of the Royal Society A* **1965,** *286*, 352-365.
30. Hoefdraad, H. E., Charge-transfer spectra of tetravalent lanthanide ions in oxides. *Journal of Inorganic and Nuclear Chemistry* **1975,** *37* (9), 1917-1921.
31. Minasian, S. G.; Batista, E. R.; Booth, C. H.; Clark, D. L.; Keith, J. M.; Kozimor, S. A.; Lukens, W. W.; Martin, R. L.; Shuh, D. K.; Stieber, S. C. E.; Tylisczcak, T.; Wen, X.-d., Quantitative Evidence for Lanthanide-Oxygen Orbital Mixing in CeO_2, PrO_2, and TbO_2. *Journal of the American Chemical Society* **2017,** *139* (49), 18052-18064.
32. Gibson, J. K.; Haire, R. G., Thermal decomposition of curium tetrafluoride and terbium tetrafluoride. *Journal of Solid State Chemistry* **1988,** *73* (2), 524-530.
33. Hinatsu, Y.; Doi, Y., Crystal structures and magnetic properties of alkali-metal lanthanide oxides A_2LnO_3 (A=Li, Na; Ln=Ce, Pr, Tb). *Journal of Alloys and Compounds* **2006,** *418* (1), 155-160.
34. El-Ghozzi, M.; Avignant, D., Crystal chemistry and magnetic structures of Tb(IV) fluorides. *Journal of Fluorine Chemistry* **2001,** *107* (2), 229-233.
35. Fulle, K.; Sanjeewa, L. D.; McMillen, C. D.; Wen, Y.; Rajamanthrilage, A. C.; Anker, J. N.; Chumanov, G.; Kolis, J. W., One-Pot Hydrothermal Synthesis of $Tb^{III}_{13}(GeO_4)_6O_7(OH)$ and $K_2Tb^{IV}Ge_2O_7$: Preparation of a Stable Terbium(4+) Complex. *Inorganic Chemistry* **2017,** *56* (11), 6044-6047.
36. Hu, Z.; Cho, E.-J.; Kaindl, G.; Müller, B. G., Valency and 4f covalency of Cs_2RbTbF_7. *Physical Review B* **1995,** *51* (12), 7514-7520.
37. Hu, Z.; Kaindl, G.; Müller, B. G., Core-level spectroscopy of the tetravalent lanthanide compounds M_3LnF_7 (with M=Cs, Rb; Ln=Ce, Pr, Nd, Tb, Dy). *Journal of Alloys and Compounds* **1997,** *246* (1), 177-185.
38. Löble, M. W.; Keith, J. M.; Altman, A. B.; Stieber, S. C. E.; Batista, E. R.; Boland, K. S.; Conradson, S. D.; Clark, D. L.; Lezama Pacheco, J.; Kozimor, S. A.; Martin, R. L.; Minasian, S. G.; Olson, A. C.; Scott, B. L.; Shuh, D. K.; Tyliszczak, T.; Wilkerson, M. P.; Zehnder, R. A., Covalency in Lanthanides. An X-ray Absorption Spectroscopy and Density Functional Theory Study of $LnCl_6^{x-}$ (x = 3, 2). *Journal of the American Chemical Society* **2015,** *137* (7), 2506-2523.
39. Su, J.; Batista, E. R.; Boland, K. S.; Bone, S. E.; Bradley, J. A.; Cary, S. K.; Clark, D. L.; Conradson, S. D.; Ditter, A. S.; Kaltsoyannis, N.; Keith, J. M.; Kerridge, A.; Kozimor, S. A.; Löble, M. W.; Martin, R. L.; Minasian, S. G.; Mocko, V.; La Pierre, H. S.; Seidler, G. T.; Shuh, D. K.; Wilkerson, M. P.; Wolfsberg, L. E.; Yang, P., Energy-Degeneracy-Driven Covalency in Actinide Bonding. *Journal of the American Chemical Society* **2018,** *140* (51), 17977-17984.
40. Bianconi, A.; Marcelli, A.; Dexpert, H.; Karnatak, R.; Kotani, A.; Jo, T.; Petiau, J., Specific intermediate-valence state of insulating 4f compounds detected by L_3 x-ray absorption. *Physical Review B* **1987,** *35* (2), 806-812.
41. Rinehart, J. D.; Fang, M.; Evans, W. J.; Long, J. R., A N_2^{3-} Radical-Bridged Terbium Complex Exhibiting Magnetic Hysteresis at 14 K. *Journal of the American Chemical Society* **2011,** *133* (36), 14236-14239.
42. Krzystek, J.; Telser, J., Insight into Electronic Properties through HFEPR Studies. In *Single-Molecule Magnets: Molecular Architectures and Building Blocks for Spintronics*, Hołyńska, M., Ed. John Wiley & Sons, Ltd.: Chichester, UK, 2018; pp 135–173.
43. Dachraoui, H.; Rupp, R. A.; Lengyel, K.; Ellabban, M. A.; Fally, M.; Corradi, G.; Kovács, L.; Ackermann, L., Photochromism of doped terbium gallium garnet. *Physical Review B* **2006,** *74* (14), 144104.
44. Gompa, T. P.; Rice, N. T.; Russo, D. R.; Aguirre Quintana, L. M.; Yik, B. J.; Bacsa, J.; La Pierre, H. S., Diethyl ether adducts of trivalent lanthanide iodides. *Dalton Transactions* **2019,** *48* (23), 8030-8033.
45. Johnson, S. A.; Kiernicki, J. J.; Fanwick, P. E.; Bart, S. C., New Benzylpotassium Reagents and Their Utility for the Synthesis of Homoleptic Uranium(IV) Benzyl Derivatives. *Organometallics* **2015,** *34* (12), 2889-2895.
46. Fulmer, G. R.; Miller, A. J. M.; Sherden, N. H.; Gottlieb, H. E.; Nudelman, A.; Stoltz, B. M.; Bercaw, J. E.; Goldberg, K. I., NMR Chemical Shifts of Trace Impurities: Common Laboratory Solvents, Organics, and Gases in Deuterated Solvents Relevant to the Organometallic Chemist. *Organometallics* **2010,** *29* (9), 2176-2179.
47. Sheldrick, G., SHELXT - Integrated space-group and crystal-structure determination. *Acta Crystallographica Section A* **2015,** *71* (1), 3-8.

48. Dolomanov, O. V.; Bourhis, L. J.; Gildea, R. J.; Howard, J. A. K.; Puschmann, H., OLEX2: a complete structure solution, refinement and analysis program. *Journal of Applied Crystallography* **2009,** *42* (2), 339-341.
49. Sheldrick, G. M., Crystal structure refinement with SHELXL. *Acta crystallographica. Section C, Structural chemistry* **2015,** *71* (Pt 1), 3-8.
50. Bruker-AXS *APEX2*, 11-0; 2014.
51. Bain, G. A.; Berry, J. F., Diamagnetic Corrections and Pascal's Constants. *Journal of Chemical Education* **2008,** *85* (4), 532.
52. Halbach, R. L.; Nocton, G.; Booth, C. H.; Maron, L.; Andersen, R. A., Cerium Tetrakis(tropolonate) and Cerium Tetrakis(acetylacetonate) Are Not Diamagnetic but Temperature-Independent Paramagnets. *Inorganic Chemistry* **2018,** *57* (12), 7290-7298.
53. George, G. N. *EDG_FIT*, Stanford Synchrotron Radiation Laboratory, Stanford Linear Accelerator Center: Stanford, CA.
54. Perdew, J. P.; Ernzerhof, M.; Burke, K., Rationale for mixing exact exchange with density functional approximations. *The Journal of Chemical Physics* **1996,** *105* (22), 9982-9985.
55. Frisch, M. J. *et. al. Gaussian 09, Revision C.01*, Gaussian, Inc., Wallingford, CT, 2009.
56. Kaupp, M.; Schleyer, P. v. R.; Stoll, H.; Preuss, H., Pseudopotential approaches to Ca, Sr, and Ba hydrides. Why are some alkaline earth MX_2 compounds bent? *The Journal of Chemical Physics* **1991,** *94* (2), 1360-1366.
57. Krishnan, R.; Binkley, J. S.; Seeger, R.; Pople, J. A., Self-consistent molecular orbital methods. XX. A basis set for correlated wave functions. *The Journal of Chemical Physics* **1980,** *72* (1), 650-654.
58. Martin, R. L., Natural transition orbitals. *The Journal of Chemical Physics* **2003,** *118* (11), 4775-4777.
59. Foster, J. P.; Weinhold, F., Natural hybrid orbitals. *Journal of the American Chemical Society* **1980,** *102* (24), 7211-7218.
60. Weinhold, F.; Landis, C., *Valency and bonding: a natural bond orbital donor acceptor perspective* Cambridge University Press 2005.
61. Dennington, R.; Keith, T. A.; Millam, J. M. *GaussView, Version 6*, Semichem Inc., Shawnee Mission, KS, 2016.
62. Lenoid, S. *Chemissian v4.60*, http://www.chemissian.com.
63. Denk, M. K.; Krause, M. J.; Niyogi, D. F.; Gill, N. K., Reaction of 1,2-dibromoethane with primary amines: formation of N,N′-disubstituted ethylenediamines $RNH–CH_2CH_2–NHR$ and homologous polyamines $RNH–[CH_2CH_2NR]_n–H$. *Tetrahedron* **2003,** *59* (38), 7565-7570.
64. King, R. B.; Sundaram, P. M., Bis(dialkylamino)phosphines. *The Journal of Organic Chemistry* **1984,** *49* (10), 1784-1789.

TOC GRAPHIC

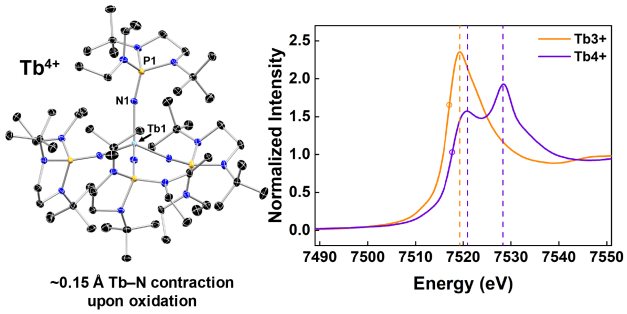
Tb4+
P1
N1
Tb1
~0.15 Å Tb–N contraction
upon oxidation
Tb3+
Tb4+
Normalized Intensity
2.5
2.0
1.5
1.0
0.5
0.0
7490
7500
7510
7520
7530
7540
7550
Energy (eV)